

**Deep learning assisted high resolution microscopy image processing for phase segmentation
in functional composite materials**

Running Head: *HIGH-RESOLUTION MICROSCOPY IMAGE PROCESSING WITH AI*

*Ganesh Raghavendran^a, Bing Han^a, Fortune Adekogbe^d, Shuang Bai^b, Bingyu Lu^a, William Wu^e,
Minghao Zhang^{a,*}, Ying Shirley Meng^{a,c,*}*

a Department of NanoEngineering, University of California San Diego, La Jolla, CA 92093

b Materials Science and Engineering, University of California San Diego, La Jolla, CA 92093

c Pritzker School of Molecular Engineering, University of Chicago, Chicago, IL 60637

d Department of Chemical and Petroleum Engineering, University of Lagos, Lagos, Nigeria
101017

e Del Norte High School, San Diego, CA, 92127

Correspondence to miz016@eng.ucsd.edu; shirleymeng@uchicago.edu

Keywords: Transmission Electron Microscopy; FFT; Deep Learning; U-Net; Li Metal; Solid
Electrolyte Interphase

■ ABSTRACT

In the domain of battery research, the processing of high-resolution microscopy images is a challenging task, as it involves dealing with complex images and requires a prior understanding of the components involved. The utilization of deep learning methodologies for image analysis has attracted considerable interest in recent years, with multiple investigations employing such techniques for image segmentation and analysis within the realm of battery research. However, the automated analysis of high-resolution microscopy images for detecting phases and components in composite materials is still an underexplored area. This work proposes a novel workflow for detecting components and phase segmentation from raw high resolution transmission electron microscopy (TEM) images using a trained U-Net segmentation model. The developed model can expedite the detection of components and phase segmentation, diminishing the temporal and cognitive demands associated with scrutinizing an extensive array of TEM images, thereby mitigating the potential for human errors. This approach presents a novel and efficient image analysis approach with broad applicability beyond the battery field and holds potential for application in other related domains characterized by phase and composition distribution, such as alloy production.

■ INTRODUCTION

In the era of information, the emphasis has transitioned from data collection to data processing. Currently, an abundance of data is accessible across various research domains, and the primary hurdle lies in extracting meaningful information through its processing. This principle holds true within the realm of materials science, where researchers endeavor to derive valuable insights from

their experimental samples, using high resolution microscopy imaging (Hill et al., 2016). The post-processing of these images has always been a challenge, owing to the complexity of the high-resolution image and the need for prior knowledge of components involved. Additionally, a comprehensive examination necessitates the acquisition of multiple images of the same sample, thereby augmenting the burden of post-processing.

In recent years, high-resolution imaging has become an indispensable tool in the field of battery material research, playing a vital role in the development of strategies to address the increasing energy demand. High-resolution transmission electron microscopy (HRTEM) stands out as a powerful technique used for investigating the microstructure of battery materials, encompassing cathodes, anodes, and electrolytes, with atomic resolution (Wang et al., 1999). Among the various battery systems under investigation, Li metal batteries have received significant attention due to their propensity to store at least 33% more power per pound than traditional Li-ion batteries, rendering them suitable for a wide range of applications, including electric vehicles, renewable energy integration, and grid-scale energy storage (Cheng et al., 2017). It is important to note that cycled Li metal, due to presence of oxides, carbonates, and sulfides, exhibits sensitivity to electron beam. Consequently, cryogenic electron microscopy (cryo-EM) technology has emerged, expanding the feasibility and necessity of high-resolution imaging in battery research, particularly for studying electron beam-sensitive anode materials like electrochemically cycled Li metal (Xu, 2014; Winter et al., 2018). Solid electrolyte interphase (SEI) formed in the anode materials after cycling is regarded as one of the least understood systems in the battery community (Li et al., 2017; Cheng et al., 2022). Studying the SEI is of scientific interest due to its crucial role in enabling long-term cycling in battery systems, as well as its complex composition of both organic and inorganic compounds. HRTEM, particularly when used in conjunction with cryogenic techniques,

enables the elucidation of the components of the thin SEI layer, which typically has a thickness in nanometer scale (Wang et al., 2017). Such characterization methods facilitate SEI engineering and the development of improved electrolyte systems.

In addition to the arduous task of sample preparation for HRTEM, processing the resulting images can also present significant challenges due to the high resolution and large amount of data produced (Taheri et al., 2016). Furthermore, *in situ* TEM studies targeting the dynamic interplay of properties, structures, and compositions within nanostructures yields substantial datasets acquired at elevated frame rates, posing an exceedingly formidable task for comprehensive data analysis (Tao & Salmeron, 2011). Recently, novel image analysis techniques have emerged within the framework of deep learning, a data processing approach that has gained tremendous popularity over the past decade. The proliferation of deep learning techniques within the field of image analysis has been spurred by several factors, such as the expanded availability of labeled datasets of significant size, notable advances in the realm of deep learning research, and the emergence of powerful high-performance frameworks like PyTorch and TensorFlow (Xue-Wen Chen & Xiaotong Lin, 2014; Badea et al., 2016).

In the field of battery research, several studies have employed machine learning and deep learning techniques for image analysis (Ling, 2022; Lombardo et al., 2022; Furat et al., 2019). The image analysis investigations have largely focused on segmenting microscopy and tomography images of electrode materials (Yao et al., 2023; Zhang et al., 2022). Automated analysis of high-resolution microscopy images for detection of phases and components in composite battery materials is an

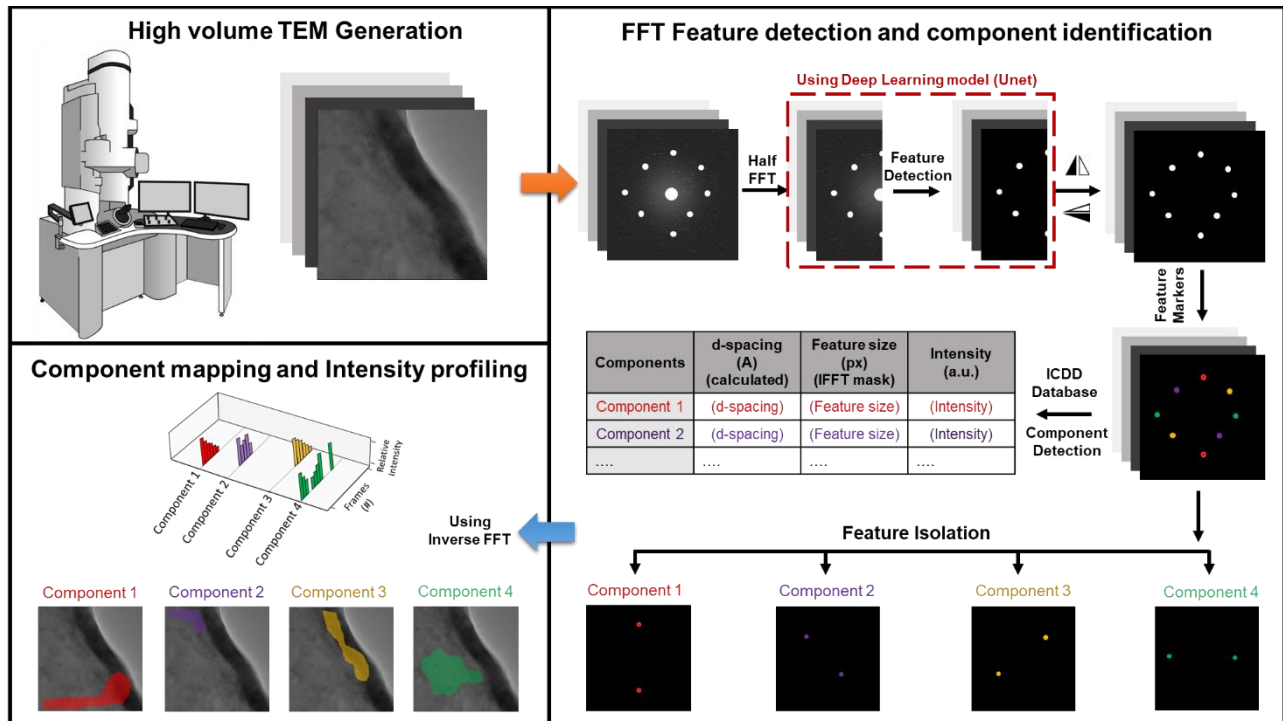


Figure 1. Schematic of the program flow – High volume of TEM data is acquired for analysis → FFT features are detected using deep learning model → Components found out from detected features using ICDD (International Centre for Diffraction Data) database → Each feature is isolated and mapped using IFFT → Component detection program is used for high volume TEM processing → Intensity profiling and mapping of components obtained.

area that remains relatively unexplored. In contrast, there have been several notable works in materials science that have focused on detecting phases and components from HRTEM images.

For instance, Liu et al. employed an unsupervised clustering algorithm combined with a scanning window technique to detect and group different phases from a TEM image of an AM Inconel 718 alloy (Liu et al., 2023). The technique can detect and map multiple phases, but there is a possibility of the same phase getting identified more than once and the chemical composition of the phases is not identified. While the method exhibits efficiency in phase mapping, its suitability for analyzing battery materials is more limited compared to alloys. Zhang et al. proposed an improved Local Contrast Attention – UNet (LCA-UNet) for detecting Fast Fourier Transform (FFT) features from TEM images of Zirconium oxides (Zhang et al., 2023). The authors utilized a scanning window technique to generate the FFT, then identified the features and labeled the corresponding phase window. The study used a 64 x 64-pixels region of the 256 x 256-pixels window for detection, potentially losing information outside the chosen region. The employed method disregarded the inclusion of asymmetrical characteristics, potentially leading to the loss of pertinent information, and the designated window was a square region rather than accurately representing the intended area. Furthermore, the intricate composition of the cycled Li metal anode samples may lead to low-contrast images that are challenging to process. In fact, using smaller-scale FFT images may exacerbate this issue, even with advanced deep learning models such as LCA-UNet.

The workflow in this study for detecting components and phase segmentation from HRTEM images is presented in **Fig. 1**. First, a FFT pattern is generated from the HRTEM image, and a trained U-Net segmentation model is used to detect features from the generated FFT image cropped half (1024 x 512 pixels). By utilizing the innate symmetry present in the FFT images, half cropped FFT images (1024 x 512 pixels) were used for model training. The half cropped FFT images performed better than the full FFT images (1024 x 1024 pixels). The d-spacing of the identified features from model generated FFT image is calculated and compared with the material

database to detect the components present in the TEM image. Finally, the inverse FFT (IFFT) image is generated for each component by masking the actual FFT image using the deep learning model, and thresholding is used to map the periodic components present in the TEM image. For high-volume TEM processing, this process is repeated for all the TEM images to be analyzed, and the intensity profile for each component is generated to observe their evolution over the imaging period. Additionally, mapping of each component is compiled into a video for visualizing the component evolution. The developed segmentation model can expedite component detection and phase segmentation, not only in the battery field but also in alloy manufacturing. The qualitative and quantitative analysis of TEM images in this work decreases the time and effort necessary for evaluating substantial quantities of TEM images while mitigating the potential for human error caused by cognitive task-induced state fatigue (Behrens et al., 2023) of analyzing a large set of TEM images (e.g ~100 images).

■ MATERIALS AND METHOD

TEM Sample Preparation:

LiF powder was ground in an Ar gas glove box and the ground LiF powder was dispersed on the TEM Cu grid. The TEM Cu grid is loaded to Melbuild vacuum transfer holder under Ar atmosphere and the sample is transferred into the TEM column without any air exposure. The experiment is performed at room temperature for beam damage analysis. For cryo temperature measurement, liquid nitrogen was added to the dewar when the holder is fully inserted into the column. The system stabilized at $\sim -165^{\circ}\text{C}$ for cryo temperature beam damage analysis.

TEM Imaging:

We used a ThermoFisher Talos F200X TEM electron microscope system with super-low-dose TEM techniques to characterize samples. The low dose HRTEM images were acquired with controllable electron dose rate ($50\text{-}1000\text{ e A}^{-2}\text{ s}^{-1}$) at FEI Ceta 16M camera and low dose system. The pixel size of the TEM image corresponds to 0.037 nm/pixel.

Automated training set generation:

The preprocessing of raw FFT images generated from HRTEM images (using opencv2 library) for the purpose of training a segmentation model involves the use of Gaussian filters, which is a standard image processing technique available in the widely used SciKit Image python package (Pedregosa et al., 2012). The training images generated through this process are produced according to specific instructions provided in the accompanying code. In contrast, the production of labeled data involves manual input from experts in the field who utilize Adobe Photoshop software to identify and mark features in the FFT images. Empirical selection of parameters, such as the standard deviation of the Gaussian kernel, is undertaken in both of these processing steps and maintained consistent across all images in the dataset. A standard deviation of 3 was used for the Gaussian kernel in the multidimensional Gaussian filter made available by SciPy.

To generate a training set for the proposed deep learning-based framework for phase identification and analysis of TEM images, a total of 80 reduced FFT images (2048 x 2048 pixels), collected during multiple experiments, were utilized. To standardize the dataset, the FFT images were resized through interpolation to a uniform resolution of 1024 x 1024 pixels. Furthermore, to increase the diversity of the dataset, the FFT images were augmented by applying affine transformations and image rotations, resulting in a total of 1986 images. To investigate the impact of both dataset size and image resolution on model accuracy, a similar data augmentation technique

was applied to generate four distinct datasets. Two datasets consisted of 1986 images each, one with a resolution of 256 x 256 pixels (resized through interpolation) and the other with 512 x 512 pixels (resized through interpolation). Additionally, two smaller datasets of 500 images each were generated with the same respective resolutions. Data augmentation of the images was performed using the ImageDataGenerator function

from the popular Tensorflow library. The affine transformations used on the images include : Rotation - Randomly rotated slightly by setting a range of ± 0.2 degrees, Horizontal Translation - Randomly shifted by up to 5% of the image's width in either the left or right direction, Shearing - Slanting the shape of an image, towards the left or right direction by 0.05 degrees, and Zooming - Randomly zoomed in or out by up to 5%. Finally, the generated images were cropped to 1024 x 512 pixels to obtain the final training set (**Fig. S1**). This approach ensures that the deep learning model is trained on a diverse range of images and can accurately identify and classify phases in TEM images.

Programming and training machine learning models:

The study employed Python for all programming activities, with the keras framework utilized for machine learning. The final dataset consisted of 1968 images with dimensions of 1024×512 pixels, randomly divided into training (90%, or 1771 images) and validation (10%, or 197 images) sets. The UNet-type architecture for segmenting 1024×512 images used in the study comprised three convolutional layers with max-pooling or up-sampling. The models were trained for 100 epochs on Dell workstations with Nvidia RTX A4000, 16GB, 4DP GPUs, with each model taking approximately 10-11 hours to train. The training period was deemed sufficient for experimentation with network architecture, data preprocessing, and hyper-parameter tuning. The stability of the models was ensured by tracking loss as a function of epoch number, indicating general

convergence. Finally, the binary segmentation map, which classified individual pixels as particle or background, was obtained by thresholding predicted softmax output for each pixel.

FFT processing for TEM images

TEM images can contain complex structures with multiple crystallographic and amorphous phases. Therefore, extracting and interpreting statistical information and uncovering the underlying physical mechanisms can pose significant challenges. FFT is useful for identifying periodic patterns in TEM images, such as lattice fringes, and for extracting information about the crystallographic orientation and symmetry of the sample (Jany et al., 2020). For this study, the Cryo-EM images of cycled Li metal anode in different electrolytes are used to introduce variability and to reduce redundancy. Images of magnification >300 kx are chosen for getting SEI layer of the anode in better resolution. The Cryo-EM images of format .dm3/.dm4 generated by GATAN micrograph software are used specifically. The TEM image is generated from the .dm3/.dm4 files using the DM3lib python library (Pierre-Ivan Raynal, 2014) and the FFT image is generated from the TEM image using FFT function from NumPy library in python. The mathematical representation of the 2D Fourier transform for an image signal $f(x,y)$, across an x-y plane can be articulated as follows:

$$F(u, v) = \frac{1}{M * N} \sum_{x=0}^{M-1} \sum_{y=0}^{N-1} f(x, y) e^{-2\pi i (\frac{ux}{M} + \frac{vy}{N})} \quad [1]$$

Here, $F(u,v)$ is the Fourier transform of $f(x,y)$, and u and v are the spatial frequencies in the x and y directions, respectively, and M , N are the width and height of the image respectively.

The integral is taken over the entire $x-y$ plane. In the field of image processing, the Fourier transform is commonly employed to analyze and manipulate the frequency components of an

image. To achieve a more visually meaningful representation, the zero-frequency component is shifted to the center of the transformed array, and the resulting complex number is converted into an absolute value. A logarithmic operation is then applied to the absolute value for perceptual scaling (Garcia-Garcia et al., 2017). This transformed matrix is subsequently converted into an intensity image containing only the logarithm of the absolute values of the complex numbers, wherein the pixel values range from 0 (representing black) to 1 (representing white). The resulting image is then cropped from the center to generate a reduced FFT image with a size of 2048 x 2048 pixels (**Fig. S2(a)**).

A factor map of dimensions 2048 x 2048 is created, where each pixel is assigned an output value based on its position and is then utilized to process the FFT images (**Fig. S2(b)**). The luminosity and contrast of the FFT images are amplified by 80% to compensate for the loss of brightness that occurs because of the application of the exponential mapping function. The resulting images are deemed suitable for further analysis and are comparable with FFT images of the same TEM image generated by GATAN (**Fig. S2(d-f)**).

Component detection using the FFT image

Circular integration is a widely used and straightforward approach for analyzing FFT images (Beaudoin & Beauchemin, 2002). The method involves dividing the FFT image into circular bands and integrating the pixel values within each band (**Fig. 2(c)**). The resulting integrated values are plotted against the real distance of each circular band, which is determined by calculating the reciprocal distance from the center of the FFT image (**Fig. S2**). To convert the reciprocal distance to real distance, the pixel size information of the TEM image file (.dm3/.dm4) is extracted using DM3lib and applied to the following formula:

$$\frac{4096 * pixelsize}{\sqrt{(x - 511.5)^2 + (y - 511.5)^2}} \quad [2]$$

Here, *pixelsize* is the calibration information obtained from GATAN software that indicates the real size of a pixel in the TEM image and (x,y) is the coordinate of the features or the circular band. The periodic components present in the TEM image can be identified by the peaks obtained from the diffraction-like graph generated using the circular integration method. The position of the peak corresponds to the d-spacing of the periodic components, aiding in the identification of the components present in the image. However, the analysis of the noisy FFT images using the circular integration method results in a diffraction-like graph that is also noisy, making it difficult to detect the peaks accurately (**Fig. S2(g-i, j)**).

Hyperparameter Tuning for U-Net model:

Hyper parameter tuning was carried out using Bayesian Optimization via the Keras Tuner Python Library. Bayesian Optimization uses probabilistic models to guide the hyper parameter search process. It is particularly useful for black box functions and problems where the objective function takes a long time to evaluate.

In this work, the objective for the optimization was minimizing the validation loss and 15 trials were allowed with 100 epochs per trial. A callback was added to the Tuner to ensure that if the model's dice coefficient did not continue to increase after 3 epochs, the training is terminated to save experimentation time.

In each trial, the optimization occurred over with respect to 6 parameters. These include the learning rate, convolutional kernel size, number of convolutional filters, convolutional transpose kernel size, activation function and 3 drop out values treated separately. The learning rate was set

to vary between three values which were $1e-4$, $1e-5$ and $1e-6$. The convolutional kernel size was set to vary between 3 and 5. The convolutional transpose kernel size was set to vary between 2 and 3. The convolutional filter was set to vary between 256 and 1024. The activation function was set to vary between ReLu, eLu and GeLu. All 3 dropout values were set to vary between 0 and 0.5 with steps of 0.1.

■ RESULTS AND DISCUSSIONS

FFT feature detection using deep learning – high resolution image segmentation

To address the noisy peaks in the diffraction-like graph, deep learning techniques are employed to detect and isolate features in the FFT image, thereby reducing the noise. Semantic segmentation is an essential technique employed in machine learning for the identification and classification of individual pixels in an image into distinct classes or entities (Kim et al., 2014). By mimicking the way in which humans perceive and analyze visual data, semantic segmentation is a fundamental step in enabling machines to comprehend and interpret micrography images accurately. In the context of micrography, semantic segmentation holds significant potential in distinguishing between different cell types or structures at the pixel level, thereby aiding in various fields, including medical diagnosis, biological research, and particle sizing (Guo et al., 2018).

U-Net architecture is a widely used deep learning technique for semantic segmentation. U-Net is composed of two main pathways, namely, the contracting and expansive paths. The contracting path focuses on capturing the context of the input image, whereas the expansive path enables precise localization by up sampling the feature maps (Ronneberger et al., 2015). The present study employs the U-Net segmentation model to detect features in the FFT image (**Fig. S4**) where very

few annotated images are used. A large set of training data and corresponding ground truth are generated using data augmentation.

In this study, to address the issue of low signal-to-noise ratio (SNR) in the FFT images, Gaussian filtering is employed. The Gaussian blur technique is particularly suitable for images that are prone to noise, as the results of filtering are relatively independent of the noise characteristics and dependent on the variance value of the Gaussian kernel (Brüllmann & d'Hoedt, 2011; Fan et al., 2019). In the context of image segmentation, this method has a limited scope and is not universally applicable (Horwath et al., 2020). Rather, its efficacy lies in its ability to accurately distinguish between features and noise to produce a more precise segmentation (Alomar et al., 2023). To optimize the training set conditions and model parameters, four factors are taken into consideration, namely, the size of the training set, resolution of the training image, the number of filters, and the threshold of the segmented image.

The impact of training set size on image classification accuracy was investigated. Models were trained on 500 and 1968 images (all 256x256 pixels) and their performance was compared (**Fig. S5**). The number of annotated images used for training a U-Net model has a significant impact on its accuracy (Caicedo et al., 2019). When using small sections of images for training, the training accuracy increases in a similar fashion as with large images, but the validation accuracy seems to be much lower after each epoch. The study suggests that decreasing the size of the input requires decreasing the capacity of the network to avoid overfitting. After training with 1968 images of 256 x 256-pixels size, the detected features were observed to be more precise and clearer (**Fig. S6(e-f)**). However, some features were observed to be missing potentially due to overfitting. (**Fig. S6(f)**) (**Fig. S8**).

A fixed training set of 1968 images was used to compare the segmentation results of 256 x 256 pixels and 512 x 512 pixels images (**Fig. S7**). It was observed that the missing features in the 256 x 256 pixels training set images were more accurately identified when the training set resolution was increased to 512 x 512 pixels (**Fig. S7(c-f)**) (**Fig. S8**) and further improved with 1024 x 1024 pixels resolution (**Fig. S9**) (**Table. S1**). However, it should be noted that using larger images would lead to increased computational cost and training time, as the U-Net model would need to process more pixels (Sabottke & Spieler, 2020). Nonetheless, the use of higher resolution images has the potential to enhance the performance of the model by capturing more details and improving generalization (Piao & Liu, 2019).

In semantic segmentation, convolutional layers with a higher number of filters can extract more complex patterns from image data effectively (Ahmed & Karim, 2020). The initial layer of filters captures basic patterns such as edges, corners, and dots, while the following layers combine these patterns to create more complex ones. Deeper layers capture more complex patterns, requiring larger combinations of patterns. Although an increase in the number of filters does not always improve semantic segmentation performance, it is still preferred over increasing the number of pooling layers. Pooling layers increase the field of view but discard "where" information, making them unsuitable for pixel-accurate labeling, which is required for semantic segmentation. Pooling layers are better suited for tasks such as object recognition, where the presence of an object in an image needs to be detected. Therefore, this study evaluates the effect of increasing filters on the semantic segmentation task. Based on our assessment, it was determined that 1024 filters yielded optimal results for segmentation.

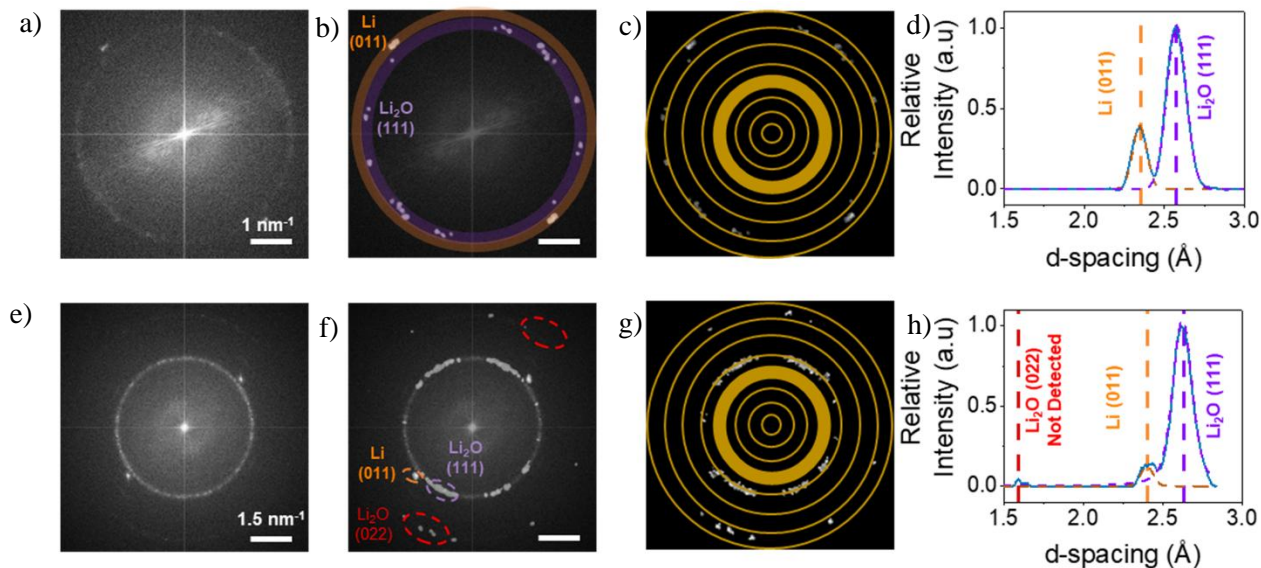


Figure 2. Image analysis of (a) computer generated FFT of TEM image of the SEI in a cycled Li metal anode: (b) detected FFT features using U-Net model trained with full (1024 x 1024 pixels) images and (c) circular integration technique on segmented image to obtain the (d) diffraction-like graph of the FFT image. Image analysis of (e) another computer generated FFT of TEM image of the SEI in a cycled Li metal anode: (f) model trained with full (1024 x 1024 pixels) images suffer from improper symmetry in segmentation (marked in dashed red) and merged features (marked in dashed purple). (g) circular integration technique on segmented image (h) failed peak detection in diffraction-like graph for low intensity features.

The U-Net model, as described previously, was utilized to detect features in the FFT image (**Fig. 2(a)**) and generate a corresponding labeled image with white markings indicating the detected features. The labeled FFT image was subsequently masked onto the original FFT image (**Fig. 2(b)**), and circular integration (**Fig. 2(c)**) was applied to generate the diffraction-like graph (**Fig. 2(d)**). An example of this process is illustrated in **Fig. 2**, where the FFT image obtained from a

TEM image of a Li metal anode was processed to obtain the diffraction-like graph. The Li (011) (2.42\AA) and Li_2O (111) (2.65\AA) components were detected using the peak positions and the ICDD database (American Society for Testing and Materials (ASTM), 1941.). The segmentation model, U-Net, was trained using 1024×1024 pixels images. However, the model suffered from poor symmetry in some cases of the resultant FFT (**Fig. 2(e)**), as demonstrated in **Fig. 2(f)** with regions marked in red dots, and imprecise segmentation due to the detected features being merged, as shown in regions marked in blue dots. Moreover, the peak detection of crystalline components using circular integration (**Fig. 2(g)**) sometimes failed at very low intensity, as shown in **Fig. 2(h)**, where the Li_2O (022) component was not detected due to the low intensity of the feature.

FFT half image training technique

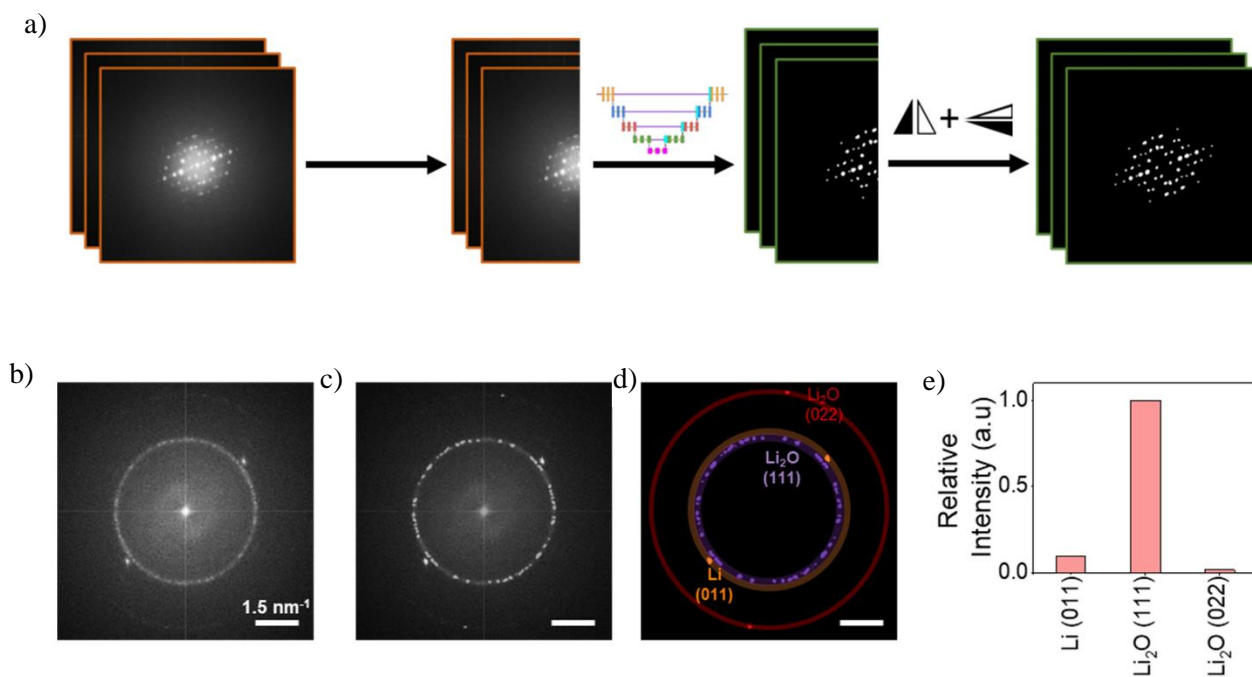


Figure 3. (a) Schematic of the usage of half FFT images for feature detection. Image analysis of (b) computer generated FFT of TEM image of the SEI in a cycled Li metal anode. (c) Model trained with half (1024×512 pixels) images preserves symmetry and produces clear distinct

features. (d) Individual features detected from the segmented image with mask for IFFT (e) Feature intensity graph generated from results of instance segmentation.

Components	d-spacing (Å) (Calculated)	d-spacing (Å) (from GATAN)	% Match	Feature size (pixels) (IFFT mask)	Pixel value count (a.u)
Li (011)	2.41641	2.416	100%	20.03	28078
Li ₂ O (111)	2.62746	2.6528	99.04%	17.31	287173
Li ₂ O (022)	1.59336	1.593	100%	11.53	4601

Table I. Tabulated results from the instance segmented image.

To address the imprecise segmentation, the symmetry of the FFT image was utilized by dividing the image into two halves, using only half of the image for training, and reducing the training image size by half to 1024 x 1024 pixels. This novel technique, though exhibiting the possibility of overfitting, is observed to perform better than the model trained with 1024 x 1024 pixels (**Fig. S10 – S12**). To tackle the issue with low intensity peak detection, the watershed segmentation algorithm was employed for image segmentation, including instance segmentation. The algorithm detects the background and foreground using morphological operations such as opening and dilation and identifies the sure foreground using distance transform. The unknown area is identified, and markers are utilized to detect the exact boundaries of the objects (Kumar et al., 2020). To obtain a complete FFT image, the half of the FFT image is first duplicated and then horizontally mirrored. The mirrored image is then rotated by 90 degrees (**Fig. 3(a)**). The challenge in processing the FFT image (**Fig. 3(b)**) using model trained with full FFT images (1024x1024 pixels) was overcome by employing a model trained on half FFT images (1024x512 pixels) for

feature detection, as shown in **Fig. 3(c)**. Instance detection using watershed segmentation was employed to detect all features (**Fig. 3(d)**) and to obtain the intensity profile after masking (**Fig. 3(e)**). Each feature detected was matched with a component from the database and averaged out to generate results. The components detected from the instance segmentation provide not only the exact position of the components detected, which agrees closely with the values generated from the GATAN Micrograph software, but also the size of the feature. This size information can be used to design masks of the appropriate size to prevent noise from the FFT from being included in the mask, and a more accurate and discrete intensity profile was obtained after masking (**Table I**).

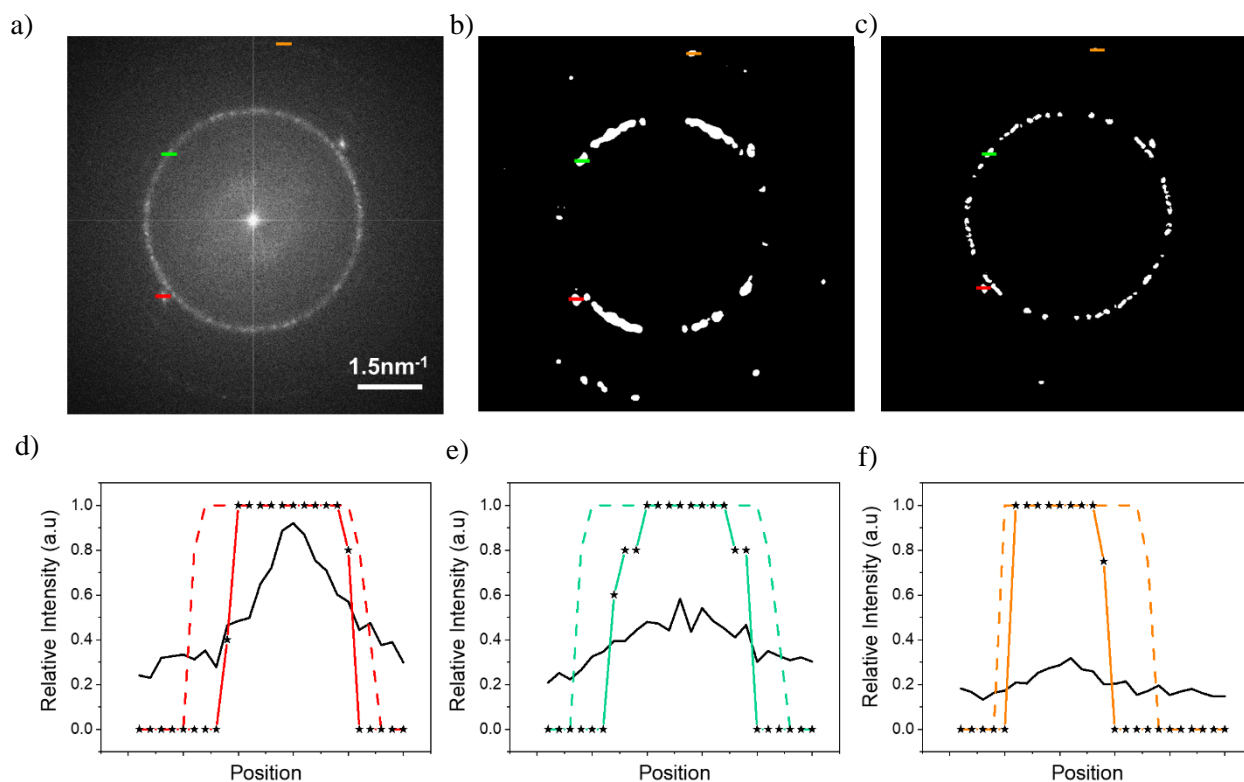


Figure 4. Intensity profiles for selected features in (a) computer generated FFT of TEM image of the SEI in a cycled Li metal anode. Line scans of three features compared with segmented images generated by (b) model trained with full (1024 x 1024 pixels) images and (c) model trained with half images (1024 x 512 pixels). (d-f) Intensity variation for each feature in the raw image (solid

black line), model trained with full (1024 x 1024 pixels) images (dashed), and model trained with half images (1024 x 512 pixels) (starred-solid).

The features detected by the model trained with full size (1024x1024 pixels) images tend to produce features at least 30% bigger than the model trained with half-size images (**Fig. 4 (a-c)**). The intensity profile shows the robustness of the new model trained with half images (**Fig. 4 (d-f)**). The size of the segmented feature is important as a larger sized feature makes the distinct features more prone to merging, resulting in inaccurate IFFT generation from the masking. Given the robust model, this tool can be used for high throughput TEM image analysis. The relative intensity distribution of the components and the mapping of the components can be achieved with the tool.

LiF beam damage analysis

The investigation of the SEI in lithium-ion batteries requires the use of TEM for atomic resolution imaging. Electron beam and environmental factors are known to cause irradiation damage in the SEI. To avoid such damage, the lithium sample must be maintained at low temperatures, but even then, the dose rate and exposure time can impact the sample's decomposition products and rate (Cheng et al., 2022). The present study aims to analyze the beam damage of lithium fluoride (LiF), which is a commonly occurring SEI component, using a high-volume TEM image processing tool. To this end, we obtained data on LiF beam damage from a study that investigated the effects of beam damage on the imaging of SEI components in a cycled lithium metal anode, while considering the dose rate and exposure time. In our study, we analyze the LiF particle's images at cryogenic and room temperatures, and with various dose rates ranging from $50 \text{ e } \text{Å}^{-2} \text{ s}^{-1}$ to 1000 e

$\text{Å}^{-2} \text{ s}^{-1}$ using the developed TEM processing methodology. The TEM images are obtained by the Mel-Build holder using an optimized workflow.

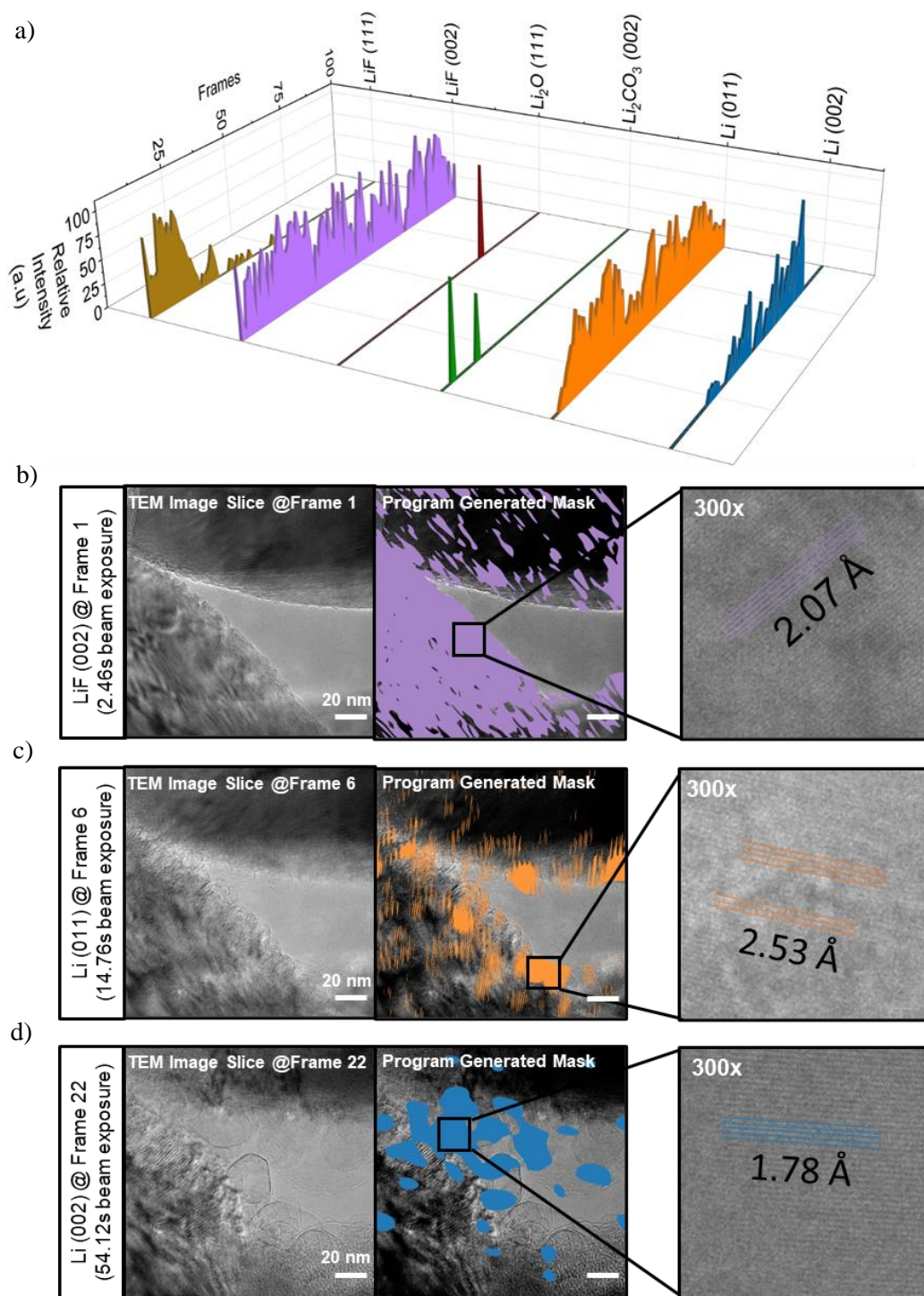


Figure 5. (a) Intensity distribution of detected components over 100 frames of LiF at electron dosage of $1000 \text{ e} \text{ \AA}^{-2} \text{ s}^{-1}$ and cryo temperature. TEM image slice and program generated IFFT mapping at the initial detection of (d) LiF (002) – after 2.46 s beam exposure, (b) Li (011) – after 14.76 s beam exposure, and (c) Li (002) – after 54.12 s of beam exposure.

A video was recorded during TEM imaging to monitor the beam damage of LiF particles. The Velox software was used to save the resulting video file in the mrc format, which contained 100 slices corresponding to 2.46 seconds of electron beam exposure each. The mrc python library (PyPi.org, 2022) was utilized to extract image data from the file, but since it was unable to retrieve the pixel size information, this information was manually entered along with the mrc file for subsequent processing. Batch file processing was employed for the automatic analysis of the components present in the sample, which were mapped using feature extraction from the FFT image. The intensity of each component was recorded and compared to its corresponding intensity in the subsequent slice to track the evolution of the components during beam damage (**Fig. 5 (a)**). This allows for effective assessment of the beam damage of LiF particles during TEM imaging. The analysis of the intensity distribution of the detected components over 100 frames of beam exposure of LiF (**Fig. 5 (a)**) reveals that the Li (011) phase diffuses out of the LiF first at 6th frame or after 14.76 s of beam exposure (**Fig. 5 (b)**). The Li (011) facet is the most commonly observed facet during nucleation, despite the slightly lower surface energy of Li (002) facet which is observed at 22nd frame or after 54.12 s of beam exposure (**Fig. 5 (c)**). This is due to the lower thermodynamic overpotential required to obtain Li (011) facet, which overpowers the surface energy effect (Nagy et al., 2019). The intensity of the Li (011) phase decreases and starts to increase midframe due to the appearance of underlying LiF particles. Li_2O (111) and Li_2CO_3 (002) phases are also observed, which could be attributed to the surrounding environment of the TEM

chamber (Liang et al., 2020). LiF (002) is dominant over LiF (111) phase because it has a lower surface energy and a higher binding energy (Chattopadhyay et al., 2012). LiF (111) is observed at the initial frames of the beam exposure (**Fig. S13**) and fades away as Li (011) phase grows. There is no information provided in literature that directly answers whether using high dose rates during TEM can convert one phase with lower surface energy to one with higher surface energy. However, it is known that high dose rates can cause radiation damage to the sample, which can affect the crystal structure and properties of the material being studied. Therefore, it is possible that high dose rates during TEM could affect the surface energy of a material, but further research is needed to determine the exact mechanism and conditions under which this could occur. The consistent intensity of the (002) peak in LiF is observed to be a result of the presence of newly formed LiF particles on the bottom surface after the degradation of the topmost LiF layer due to beam damage. This observation is corroborated by the increase in the intensity of the Li (011) phase, which subsequently decreases but then increases again. The increase in the intensity of the Li (011) phase is indicative of the formation of Li (011) due to the degradation and resurfacing of LiF particles. The degradation of LiF into Li is observed to be very limited at low dose rate and at cryo temperature (**Fig. S13**). A Python-based GUI tool has been designed and developed for future use and broader distribution. This intuitive interface offers a potential advantage over current state-of-the-art analysis programs, particularly when dealing with large datasets. The GUI aims to streamline the analysis workflow, making the program's advanced capabilities accessible to a wider range of users and facilitating efficient processing of complex TEM data (**Fig. S14**).

■ CONCLUSIONS

This paper introduces a novel deep learning-based framework for identifying and evaluating the phases present in TEM images of the SEI. The framework utilizes the FFT patterns of the TEM

images to analyze the feature positions and determine the SEI components. The proposed method also incorporates techniques to handle high-resolution images and exploit the symmetry of the FFT patterns for better model performance. The framework's effectiveness is further improved by introducing additional training data. Additionally, a comprehensive analysis of the TEM images through intensity profiling and component mapping provides valuable insights into the SEI component evolution during imaging.

In future studies, we propose utilizing the diffraction pattern generated from high frame rate TEM image patches for more detailed and accurate analysis. This alternative approach is superior to the sliding window technique for generating FFT patterns from TEM images as the latter may lack clarity and clear features. Furthermore, our proposed deep learning model can be applied to analyze not only the SEI components of Li metal anodes, but also other composite systems involving periodic components (Na metal anodes, Si anodes, etc.) provided an appropriate database with the respective compounds is used. The developed workflow can be further improved by integrating it for operando detection and mapping of the phases, thereby enabling the analysis of component evolution during TEM imaging.

■ SUPPLEMENTARY INFORMATION

The Supplementary Information is available free of charge.

The Supplementary Information contains details of the optimization of the model.

■ AUTHOR INFORMATION

Corresponding Author

*(MZ) E-Mail: miz016@eng.ucsd.edu

*(YSM.) E-mail: shirleymeng@uchicago.edu

ORCID:

Minghao Zhang: 0009-0002-8303-3942

Ying Shirley Meng: 0000-0001-8936-8845

■ ACKNOWLEDGEMENTS

This work is supported by the funding and collaboration agreement between UCSD and Thermo Fisher Scientific on Advanced Characterization of Energy Materials. TEM was performed at the San Diego Nanotechnology Infrastructure (SDNI), a member of the National Nanotechnology Coordinated Infrastructure, which is supported by the National Science Foundation (grant ECCS-1542148). The workstation to build the model was provided by the University of Chicago under YSM's startup package. F.A. acknowledges support from the Research Experience for Nigerian Engineering Undergraduates (RENEU) program at the University of Chicago.

■ AUTHOR CONTRIBUTIONS

G.R., M.Z., and Y.S.M. conceived the ideas. B.H. and S.B. performed TEM imaging. G.R. and F.A developed the model for TEM processing. G.R, F.A and W.W worked on the development of GUI application. All authors discussed the results and commented on the manuscript.

■ **COMPETING INTERESTS**

All authors declare no financial or non-financial competing interests.

■ **DATA AVAILABILITY**

The datasets generated and/or analysed during the current study are available in the *TEMGUILESC* Github repository (<https://github.com/ganyguru/TEMGUILESC>).

■ **CODE AVAILABILITY**

The underlying code and training/validation datasets for this study is available in *TEMGUILESC* Github and can be accessed via this link (<https://github.com/ganyguru/TEMGUILESC>).

REFERENCES

- AHMED, W. S. & KARIM, A. AMIR A. (2020). The Impact of Filter Size and Number of Filters on Classification Accuracy in CNN. In *2020 International Conference on Computer Science and Software Engineering (CSASE)*, pp. 88–93. IEEE.
- ALOMAR, K., AYSEL, H. I. & CAI, X. (2023). Data Augmentation in Classification and Segmentation: A Survey and New Strategies. *Journal of Imaging* **9**, 46.
- AMERICAN SOCIETY FOR TESTING AND MATERIALS (ASTM) (1941). International Centre for Diffraction Data . <https://www.icdd.com/>.
- BADEA, M. S., FELEA, I. I., FLOREA, L. M. & VERTAN, C. (2016). The use of deep learning in image segmentation, classification and detection.
- BEAUDOIN, N. & BEAUCHEMIN, S. S. (2002). An accurate discrete Fourier transform for image processing. In *Object recognition supported by user interaction for service robots*, pp. 935–939. IEEE Comput. Soc.
- BEHRENS, M., GUBE, M., CHAABENE, H., PRIESKE, O., ZENON, A., BROSCHEID, K.-C., SCHEGA, L., HUSMANN, F. & WEIPPERT, M. (2023). Fatigue and Human Performance: An Updated Framework. *Sports Medicine* **53**, 7–31.
- BRÜLLMANN, D. & D’HOEDT, B. (2011). The modulation transfer function and signal-to-noise ratio of different digital filters: a technical approach. *Dentomaxillofacial Radiology* **40**, 222–229.
- CAICEDO, J. C., ROTH, J., GOODMAN, A., BECKER, T., KARHOHS, K. W., BROISIN, M., MOLNAR, C., MCQUIN, C., SINGH, S., THEIS, F. J. & CARPENTER, A. E. (2019). Evaluation of Deep Learning Strategies for Nucleus Segmentation in Fluorescence Images. *Cytometry Part A* **95**, 952–965.
- CHATTOPADHYAY, S., LIPSON, A. L., KARMEL, H. J., EMERY, J. D., FISTER, T. T., FENTER, P. A., HERSAM, M. C. & BEDZYK, M. J. (2012). In Situ X-ray Study of the Solid Electrolyte Interphase (SEI) Formation on Graphene as a Model Li-ion Battery Anode. *Chemistry of Materials* **24**, 3038–3043.
- CHENG, D., LU, B., RAGHAVENDRAN, G., ZHANG, M. & MENG, Y. S. (2022). Leveraging cryogenic electron microscopy for advancing battery design. *Matter* **5**, 26–42.
- CHENG, X.-B., ZHANG, R., ZHAO, C.-Z. & ZHANG, Q. (2017). Toward Safe Lithium Metal Anode in Rechargeable Batteries: A Review. *Chemical Reviews* **117**, 10403–10473.
- FAN, L., ZHANG, F., FAN, H. & ZHANG, C. (2019). Brief review of image denoising techniques. *Visual Computing for Industry, Biomedicine, and Art* **2**, 7.
- FURAT, O., WANG, M., NEUMANN, M., PETRICH, L., WEBER, M., KRILL, C. E. & SCHMIDT, V. (2019). Machine Learning Techniques for the Segmentation of Tomographic Image Data of Functional Materials. *Frontiers in Materials* **6**, 145.
- GARCIA-GARCIA, A., ORTS-ESCOLANO, S., OPREA, S., VILLENA-MARTINEZ, V. & GARCIA-RODRIGUEZ, J. (2017). A Review on Deep Learning Techniques Applied to Semantic Segmentation.

- GUO, Y., LIU, Y., GEORGIU, T. & LEW, M. S. (2018). A review of semantic segmentation using deep neural networks. *International Journal of Multimedia Information Retrieval* **7**, 87–93.
- HILL, J., MULHOLLAND, G., PERSSON, K., SESHADRI, R., WOLVERTON, C. & MEREDIG, B. (2016). Materials science with large-scale data and informatics: Unlocking new opportunities. *MRS Bulletin* **41**, 399–409.
- HORWATH, J. P., ZAKHAROV, D. N., MÉGRET, R. & STACH, E. A. (2020). Understanding important features of deep learning models for segmentation of high-resolution transmission electron microscopy images. *npj Computational Materials* **6**, 108.
- JANY, B. R., JANAS, A. & KROK, F. (2020). Automatic microscopic image analysis by moving window local Fourier Transform and Machine Learning. *Micron* **130**, 102800.
- KIM, J.-G., YOO, S. J., KIM, C.-Y. & JOU, H.-T. (2014). Circular Fast Fourier Transform Application: A Useful Script for Fast Fourier Transform Data Analysis of High-resolution Transmission Electron Microscopy Image. *Applied Microscopy* **44**, 138–143.
- KUMAR, N., VERMA, R., ANAND, D., ZHOU, Y., ONDER, O. F., TSOUGENIS, E., CHEN, H., HENG, P.-A., LI, J., HU, Z., WANG, YUNZHI, KOOHBANANI, N. A., JAHANIFAR, M., TAJEDDIN, N. Z., GOOYA, A., RAJPOOT, N., REN, X., ZHOU, S., WANG, Q., SHEN, D., YANG, C.-K., WENG, C.-H., YU, W.-H., YEH, C.-Y., YANG, S., XU, S., YEUNG, P. H., SUN, P., MAHBOD, A., SCHAEFER, G., ELLINGER, I., ECKER, R., SMEDBY, O., WANG, C., CHIDESTER, B., TON, T.-V., TRAN, M.-T., MA, JIAN, DO, M. N., GRAHAM, S., VU, Q. D., KWAK, J. T., GUNDA, A., CHUNDURI, R., HU, C., ZHOU, X., LOTFI, D., SAFDARI, R., KASCENAS, A., O'NEIL, A., ESCHWEILER, D., STEGMAIER, J., CUI, Y., YIN, B., CHEN, K., TIAN, X., GRUENING, P., BARTH, E., ARBEL, E., REMER, I., BEN-DOR, A., SIRAZITDINOVA, E., KOHL, M., BRAUNEWELL, S., LI, Y., XIE, X., SHEN, L., MA, JUN, BAKSI, K. DAS, KHAN, M. A., CHOO, J., COLOMER, A., NARANJO, V., PEI, L., IFTEKHARUDDIN, K. M., ROY, K., BHATTACHARJEE, D., PEDRAZA, A., BUENO, M. G., DEVANATHAN, S., RADHAKRISHNAN, S., KODUGANTY, P., WU, Z., CAI, G., LIU, X., WANG, YUQIN & SETHI, A. (2020). A Multi-Organ Nucleus Segmentation Challenge. *IEEE Transactions on Medical Imaging* **39**, 1380–1391.
- LI, YUZHANG, LI, YANBIN, PEI, A., YAN, K., SUN, Y., WU, C.-L., JOUBERT, L.-M., CHIN, R., KOH, A. L., YU, Y., PERRINO, J., BUTZ, B., CHU, S. & CUI, Y. (2017). Atomic structure of sensitive battery materials and interfaces revealed by cryo-electron microscopy. *Science* **358**, 506–510.
- LIANG, C., ZHANG, X., XIA, S., WANG, Z., WU, J., YUAN, B., LUO, X., LIU, WEIYAN, LIU, WEI & YU, Y. (2020). Unravelling the room-temperature atomic structure and growth kinetics of lithium metal. *Nature Communications* **11**, 5367.
- LING, C. (2022). A review of the recent progress in battery informatics. *npj Computational Materials* **8**, 33.
- LIU, S., AMIN-AHMADI, B., LIU, R., ZHENG, Q. & ZHANG, X. (2023). Automated phase segmentation and quantification of high-resolution TEM image for alloy design. *Materials Characterization* **199**, 112779.
- LOMBARDO, T., DUQUESNOY, M., EL-BOUYSIDY, H., ÁRÉN, F., GALLO-BUENO, A., JØRGENSEN, P. B., BHOWMIK, A., DEMORTIÈRE, A., AYERBE, E., ALCAIDE, F., REYNAUD, M., CARRASCO, J., GRIMAUD, A., ZHANG, C., VEGGE, T., JOHANSSON, P. & FRANCO, A. A. (2022). Artificial Intelligence Applied to Battery Research: Hype or Reality? *Chemical Reviews* **122**, 10899–10969.

- NAGY, K. S., KAZEMIABNAVI, S., THORNTON, K. & SIEGEL, D. J. (2019). Thermodynamic Overpotentials and Nucleation Rates for Electrodeposition on Metal Anodes. *ACS Applied Materials & Interfaces* **11**, 7954–7964.
- PEDREGOSA, F., VAROQUAUX, G., GRAMFORT, A., MICHEL, V., THIRION, B., GRISEL, O., BLONDEL, M., MÜLLER, A., NOTHMAN, J., LOUPPE, G., PRETTENHOFER, P., WEISS, R., DUBOURG, V., VANDERPLAS, J., PASSOS, A., COURNAPEAU, D., BRUCHER, M., PERROT, M. & DUCHESNAY, É. (2012). Scikit-learn: Machine Learning in Python.
- PIAO, S. & LIU, J. (2019). Accuracy Improvement of UNet Based on Dilated Convolution. *Journal of Physics: Conference Series* **1345**, 052066.
- PIERRE-IVAN RAYNAL (2014). DM3 Python Reader. <https://bitbucket.org/piraynal/pydm3reader>.
- PYPI.ORG (n.d.). mrcfile 1.4.3 Library. <https://pypi.org/project/mrcfile/>.
- RONNEBERGER, O., FISCHER, P. & BROX, T. (2015). U-Net: Convolutional Networks for Biomedical Image Segmentation.
- SABOTTKE, C. F. & SPIELER, B. M. (2020). The Effect of Image Resolution on Deep Learning in Radiography. *Radiology: Artificial Intelligence* **2**, e190015.
- TAHERI, M. L., STACH, E. A., ARSLAN, I., CROZIER, P. A., KABIUS, B. C., LAGRANGE, T., MINOR, A. M., TAKEDA, S., TANASE, M., WAGNER, J. B. & SHARMA, R. (2016). Current status and future directions for in situ transmission electron microscopy. *Ultramicroscopy* **170**, 86–95.
- TAO, F. (FENG) & SALMERON, M. (2011). In Situ Studies of Chemistry and Structure of Materials in Reactive Environments. *Science* **331**, 171–174.
- WANG, H., JANG, Y., HUANG, B., SADOWAY, D. R. & CHIANG, Y. (1999). TEM Study of Electrochemical Cycling-Induced Damage and Disorder in LiCoO₂ Cathodes for Rechargeable Lithium Batteries. *Journal of The Electrochemical Society* **146**, 473–480.
- WANG, X., ZHANG, M., ALVARADO, J., WANG, S., SINA, M., LU, B., BOUWER, J., XU, W., XIAO, J., ZHANG, J.-G., LIU, J. & MENG, Y. S. (2017). New Insights on the Structure of Electrochemically Deposited Lithium Metal and Its Solid Electrolyte Interphases via Cryogenic TEM. *Nano Letters* **17**, 7606–7612.
- WINTER, M., BARNETT, B. & XU, K. (2018). Before Li Ion Batteries. *Chemical Reviews* **118**, 11433–11456.
- XU, K. (2014). Electrolytes and Interphases in Li-Ion Batteries and Beyond. *Chemical Reviews* **114**, 11503–11618.
- XUE-WEN CHEN & XIAOTONG LIN (2014). Big Data Deep Learning: Challenges and Perspectives. *IEEE Access* **2**, 514–525.
- YAO, W., CHOUCANE, M., LI, W., BAI, S., LIU, Z., LI, L., CHEN, A. X., SAYAHPOUR, B., SHIMIZU, R., RAGHAVENDRAN, G., SCHROEDER, M. A., CHEN, Y.-T., TAN, D. H. S., SREENARAYANAN, B., WATERS, C. K., SICHLER, A., GOULD, B., KOUNTZ, D. J., LIPOMI, D. J., ZHANG, M. & MENG, Y. S. (2023). A 5 V-class cobalt-free battery cathode with high loading enabled by dry coating. *Energy & Environmental Science* **16**, 1620–1630.

ZHANG, M., CHOUCANE, M., SHOJAEE, S. A., WINIARSKI, B., LIU, Z., LI, L., PELAPUR, R., SHODIEV, A., YAO, W., DOUX, J.-M., WANG, S., LI, Y., LIU, C., LEMMENS, H., FRANCO, A. A. & MENG, Y. S. (2023). Coupling of Multiscale Imaging Analysis and Computational Modeling for Understanding Thick Cathode Degradation Mechanisms. *Joule* **7.1**, 201-220.

ZHANG, Q., BAI, R., PENG, B., WANG, Z. & LIU, Y. (2023). FFT pattern recognition of crystal HRTEM image with deep learning. *Micron* **166**, 103402.

SUPPLEMENTARY INFORMATION

Deep learning assisted high resolution microscopy image processing for phase segmentation in composite materials

Running Head : *HIGH-RESOLUTION MICROSCOPY IMAGE PROCESSING WITH AI*

*Ganesh Raghavendran^a, Bing Han^a, Fortune Adekogbe^d, Shuang Bai^b, Bingyu Lu^a, William Wu^e,
Minghao Zhang^{a,*}, Ying Shirley Meng^{a,c,*}*

a Department of NanoEngineering, University of California San Diego, La Jolla, CA 92093

b Materials Science and Engineering, University of California San Diego, La Jolla, CA 92093

c Pritzker School of Molecular Engineering, University of Chicago, Chicago, IL 60637

d Department of Chemical and Petroleum Engineering, University of Lagos, Lagos, Nigeria
101017

e Del Norte High School, San Diego, CA, 92127

Correspondence to miz016@eng.ucsd.edu; shirleymeng@uchicago.edu

Keywords: Transmission Electron Microscopy; Deep Learning; U-Net; Li Metal; Solid
Electrolyte Interphase

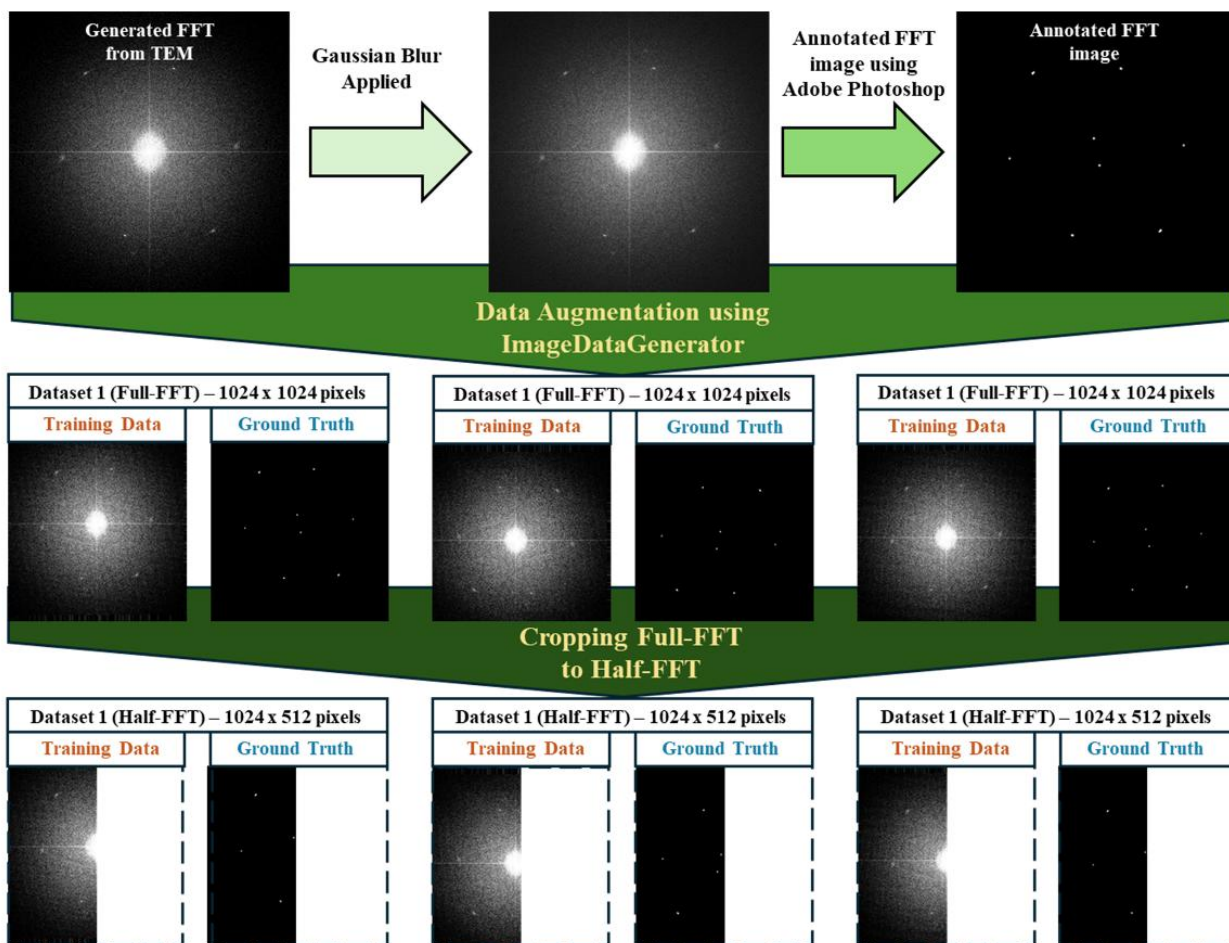


Figure S1. Schematic of the data generation for training the model.

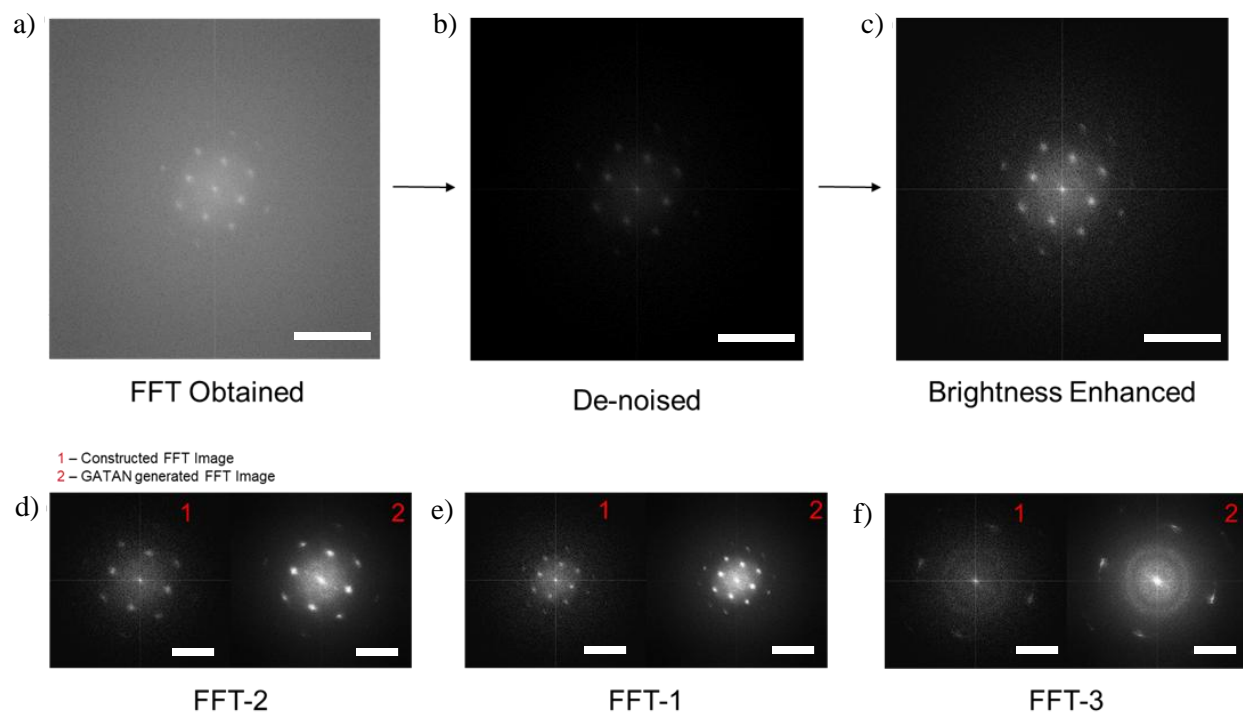


Figure S2. (a) Initial FFT image obtained from TEM using python. (b) De-noised FFT image. (c) Enhanced FFT image ready for further analysis. (d-f) Comparison of python generated FFT image (1) with GATAN generated FFT image (2) (Scale bar: $1/10 \text{ nm}^{-1}$).

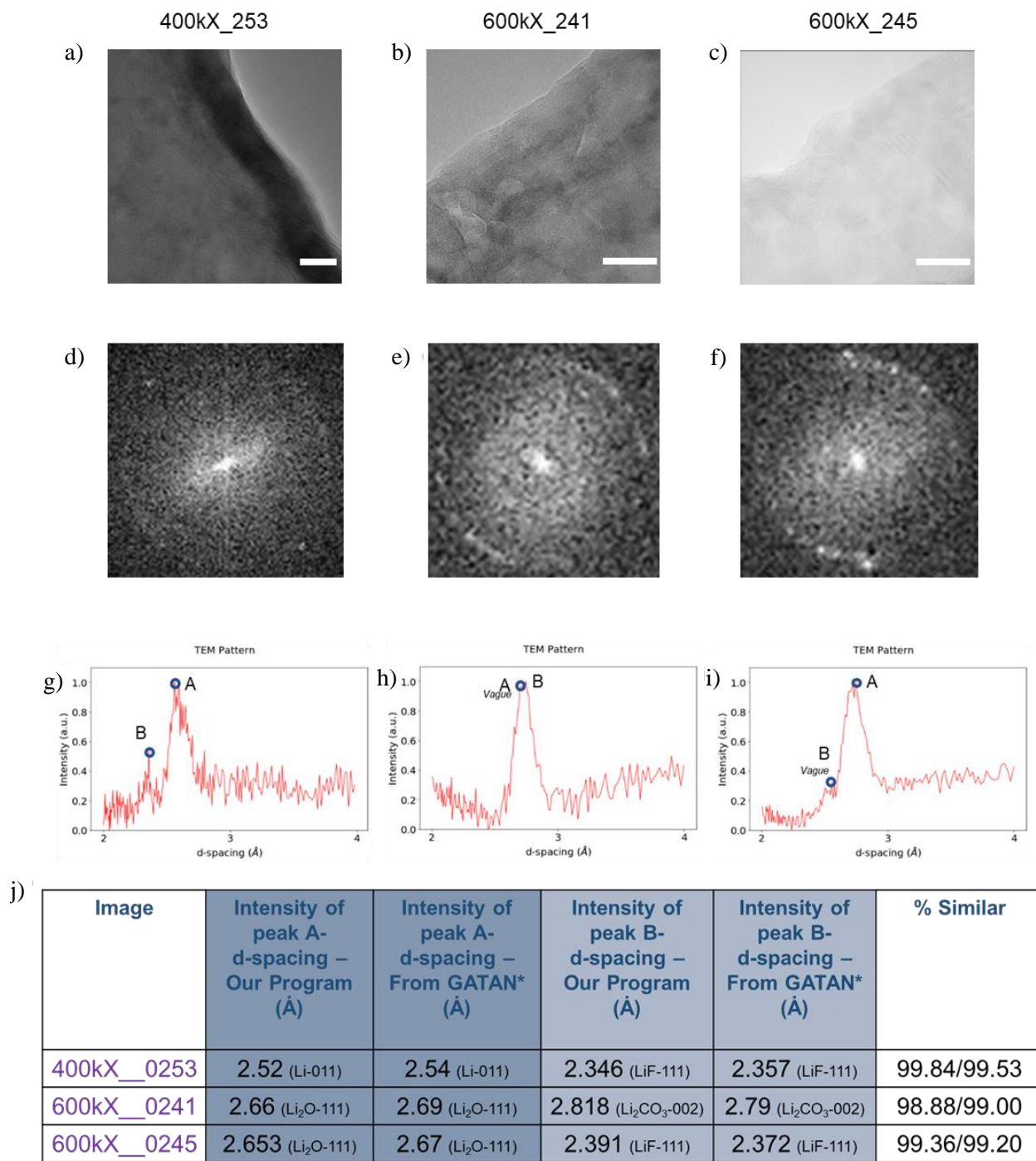


Figure S3. (a-c) TEM images (scale bar: 10 nm) of SEI of cycled Li metal anodes. (d-f) FFT images generated for corresponding TEM images. (g-i) Diffraction-like graph generated using circular reintegration method. (j) Tabulated results obtained by manually identifying the peaks and compared with d-spacing obtained from GATAN software.

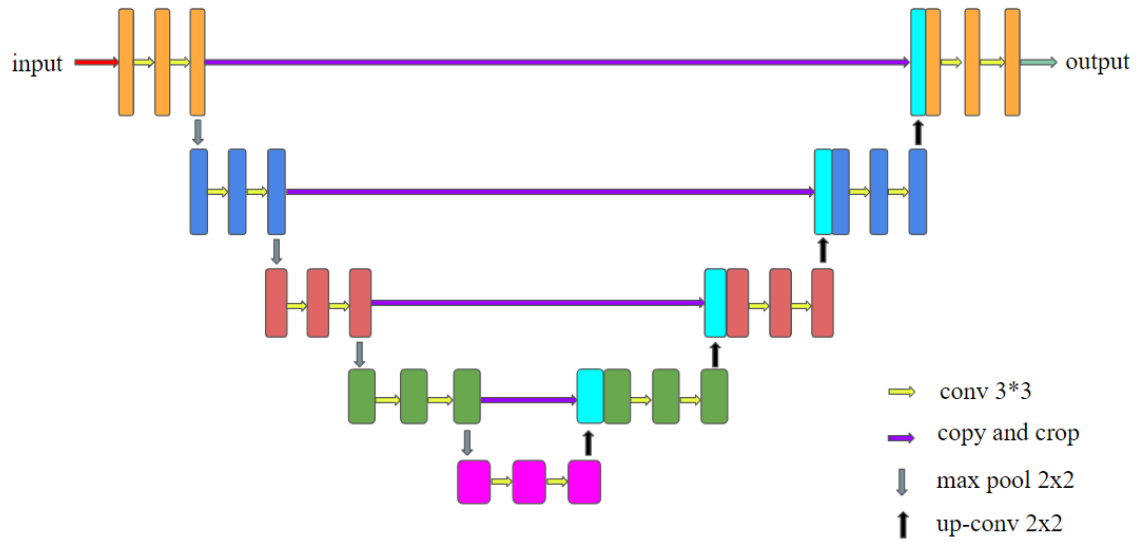


Figure S4. Schematic representation of the UNet-type architecture used on 1024x1024 pixel and 1024x512 pixel images.

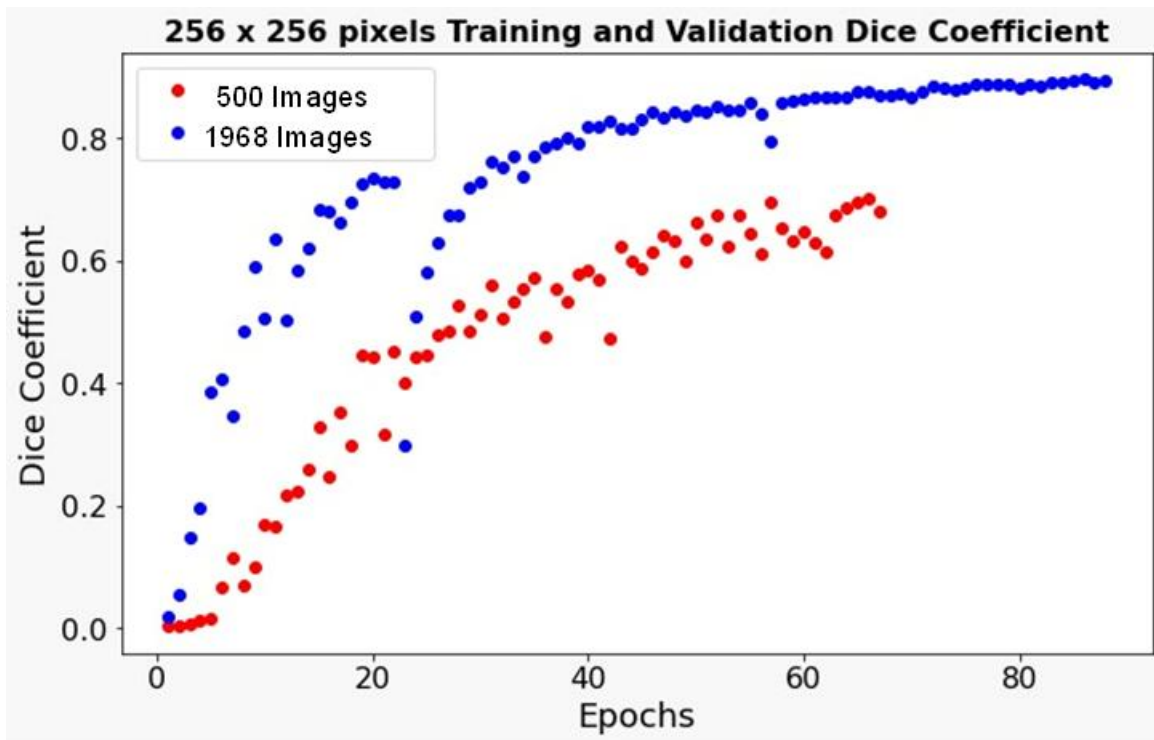


Figure S5. 1968 images based training of 256 x 256 pixels images show better performance (Dice coefficient) than 500 images based training.

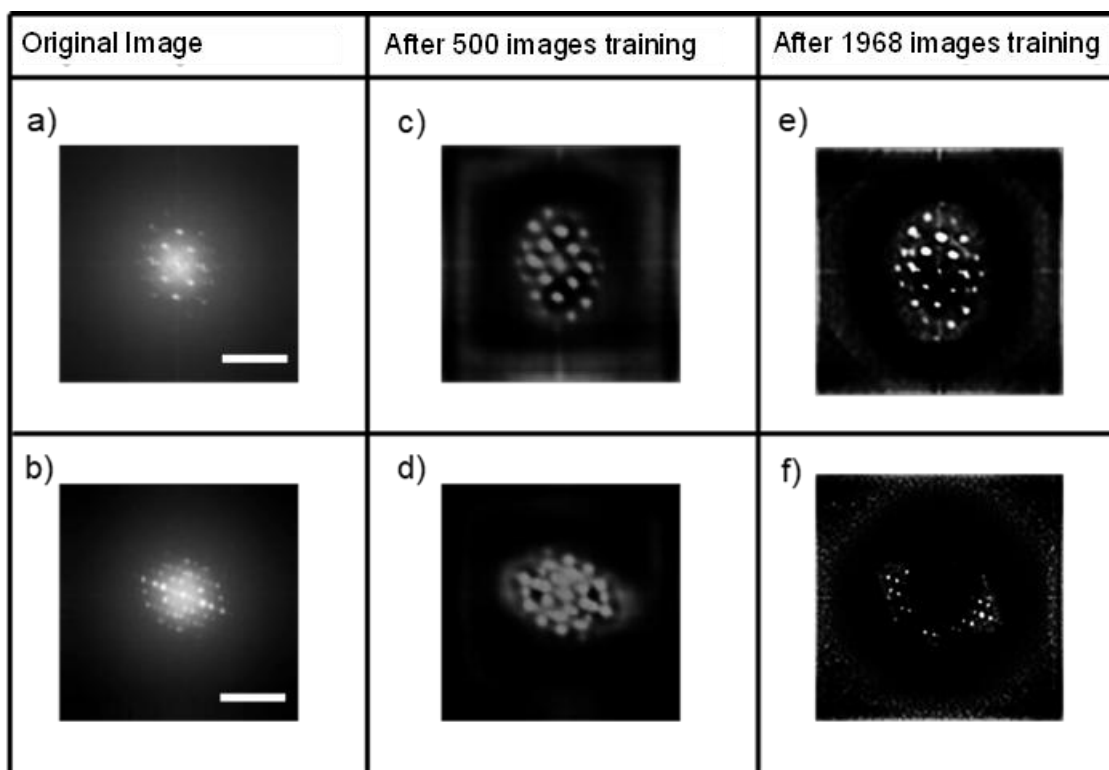


Figure S6. (a-b) Generated FFT of the TEM images of SEI of cycled Li metal anodes (scale bar: $1/10\text{nm}^{-1}$). (c-d) Segmentation images generated using 500 **FFT** images. (e-f) Segmentation images generated using **1968 FFT** images.

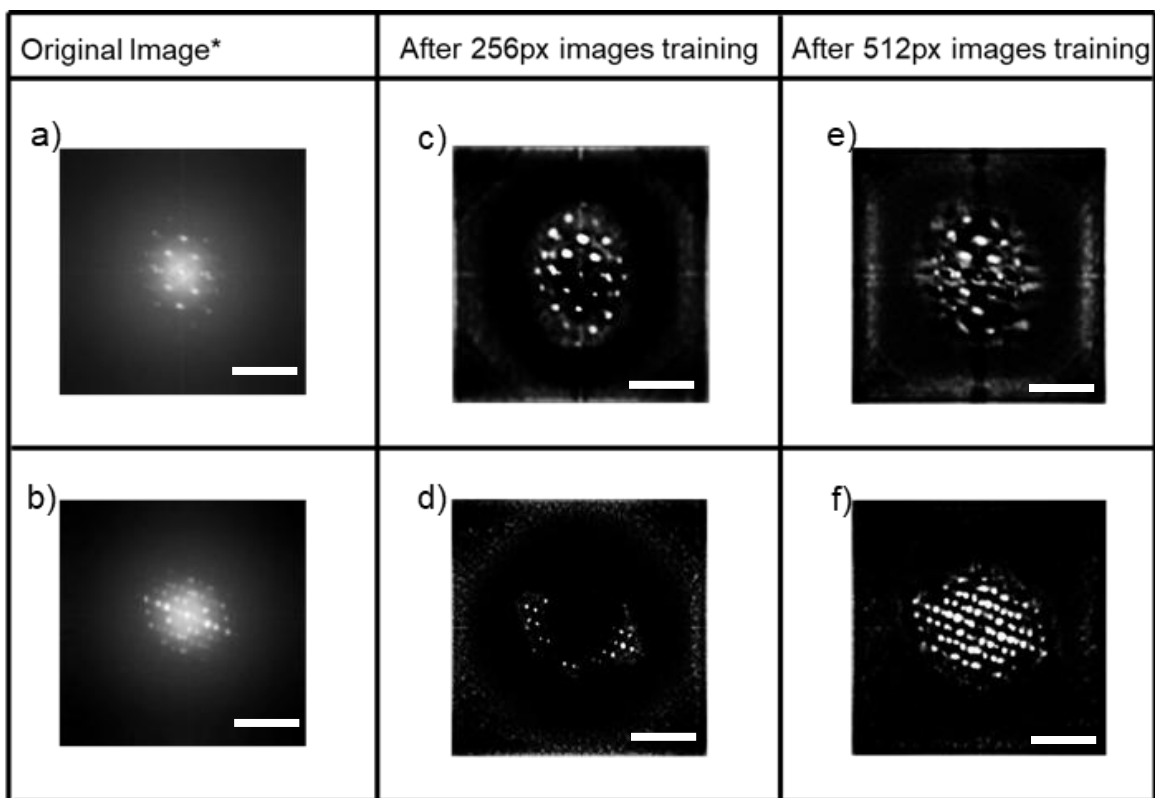


Figure S7. (a-b) Generated FFT of the TEM images of SEI of cycled Li metal anodes (Scale bar: $1/10 \text{ nm}^{-1}$). (c-d) Segmentation images generated using 256 x 256 pixels images. (e-f) Segmentation images generated using 512 x 512 pixels images.

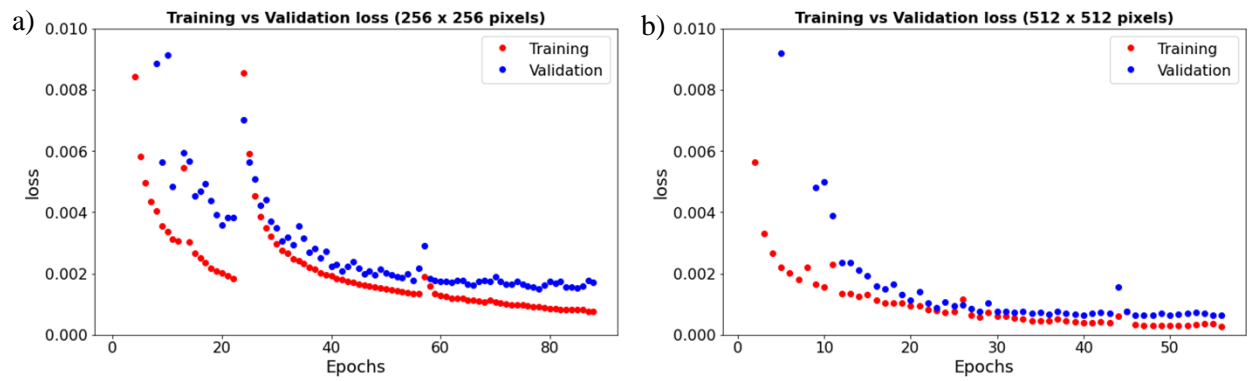


Figure S8. Training vs Validation loss of the model trained with (a) 1024 x 512 pixels and (b) 1024 x 1024 pixels.

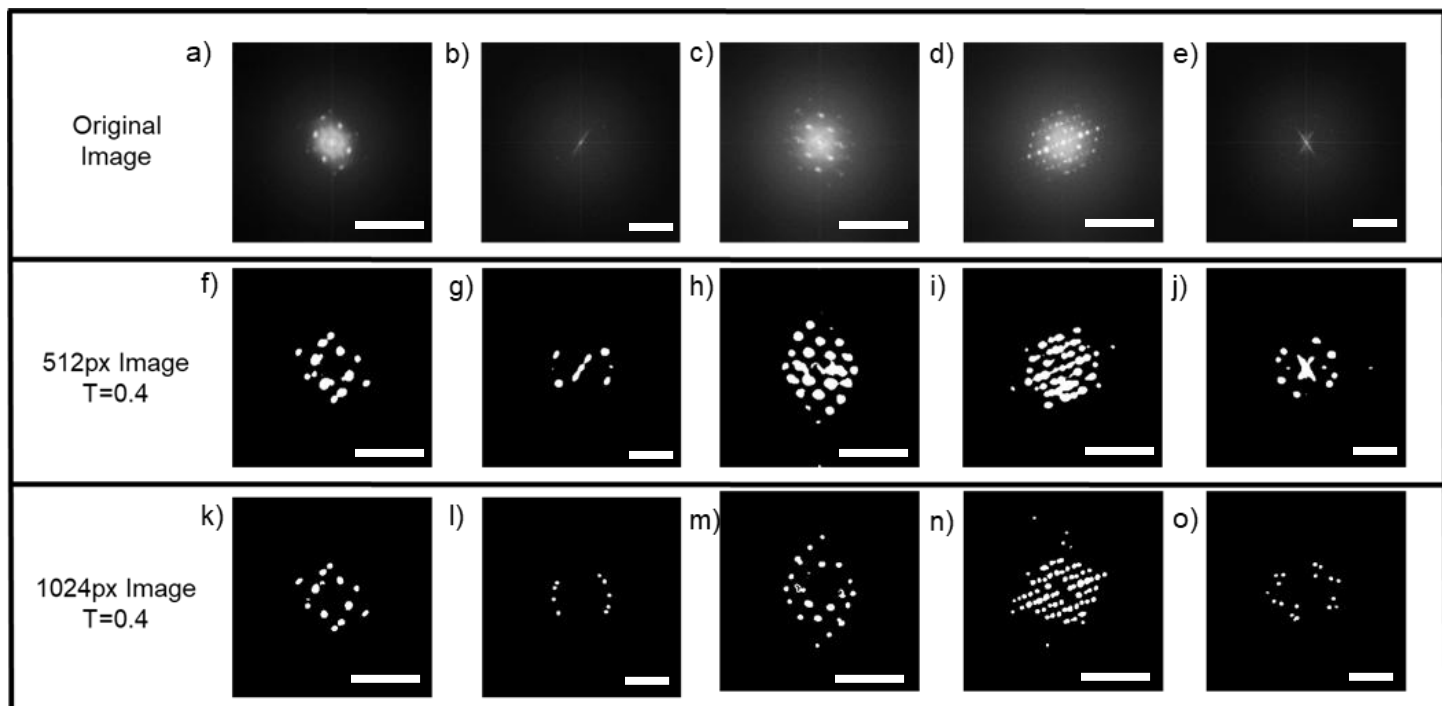


Figure S9. (a-e) Generated FFT of the TEM images of SEI of cycled Li metal anodes (scale bar: $1/10 \text{ nm}^{-1}$). (f-j) Segmentation images generated using corresponding 512x512 pixel TEM images. (k-o) Segmentation images generated using corresponding 1024x1024 pixel TEM images.

Model Name	Image size	Validation Dice coefficient	Test Dice Coefficient
U-Net	256 x 256 pixels	0.8944	0.6048
U-Net	1024 x 1024 pixels	0.9459	0.7557

Table S1. Performance metrics comparing the model performance with varying image resolution and 1024 filters

Model Evaluation Metrics

A test data set of 9 unseen FFT images (Test data) and their corresponding ground truth were used for gauging and comparing the metrics of the model. The ground truth was prepared in the similar fashion as mentioned in the data preparation section. The validation data used and the results obtained are also available in the Github repo.

Comparative Analysis of Training and Validation Loss:

The training loss vs. validation loss curve reveals a notable difference in behavior between the two models. The model trained on 1024 x 512 pixels images exhibits a slightly larger gap between training and validation loss compared to the model trained on 1024 x 1024 pixels images. This observation suggests a potential for overfitting in the model trained on smaller images.

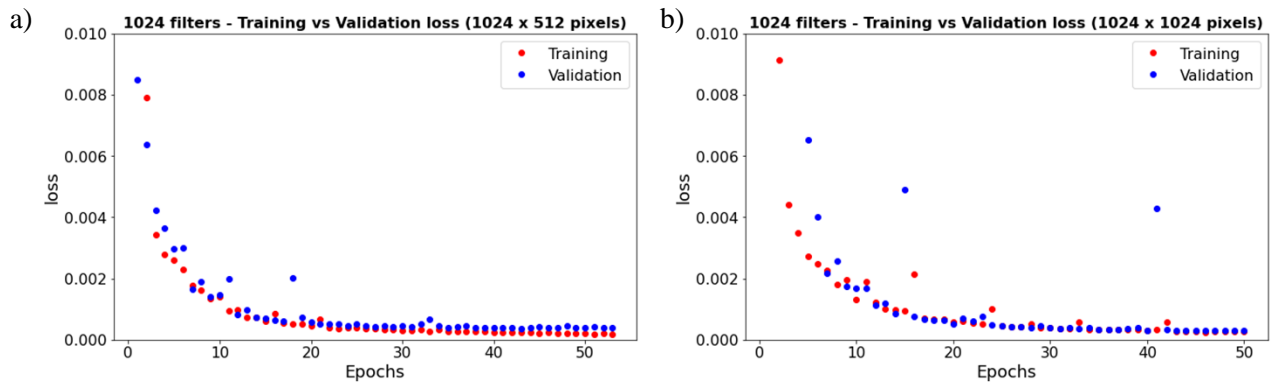


Figure S10. Confusion matrix of the validation results obtained from models trained with (a) 1024 x 1024 pixels images and (b) 1024 x 512 pixels images

Comparative Analysis of Confusion Matrices:

The confusion matrix reveals a higher incidence of false positives in the 1024 x 1024 pixels images. This could potentially complicate Inverse Fast Fourier Transform (IFFT) mapping due to larger feature sizes. Although the confusion matrix for the 1024 x 512 pixels images is based on half the number of pixels, doubling the label counts still results in lower false positives ($2 * 2483 = 4969 < 7086$) for this model. These validation results align with the findings presented in **Figure 4** of the manuscript. The results used for the generation of the confusion matrix was not threshold applied. The pixel values range of the output range from 0-1.

The model trained with 1024 x 512 pixels images have more false negatives ($2 * 3 = 6$) compared to the model trained with 1024 x 1024 pixels images, indicating a potential overfitting which aligns with the observation from training loss vs validation loss curve.

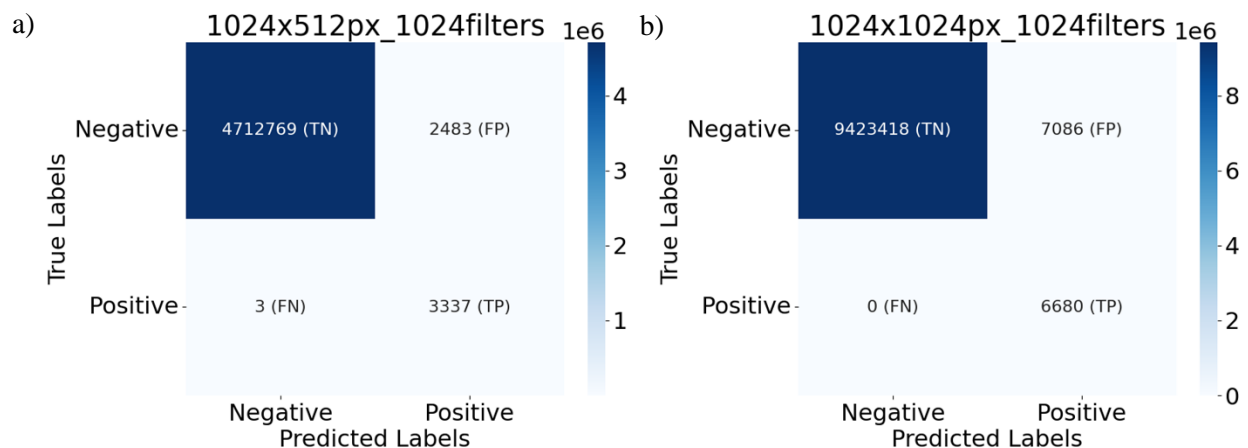


Figure S11. Confusion matrix of the validation results obtained from models trained with (a) 1024 x 512 pixels images and (b) 1024 x 1024 pixels images

Comparative Analysis of Dice scores distribution:

The image below presents the validation results without applying a threshold, with pixel values ranging from 0 to 1. Notably, the model trained on 1024 x 512 pixels images demonstrates consistently higher Dice coefficients than the model trained on 1024 x 1024 pixels images. This observation suggests that the reduced image dimensions may be advantageous for improving the model's segmentation performance and accuracy.

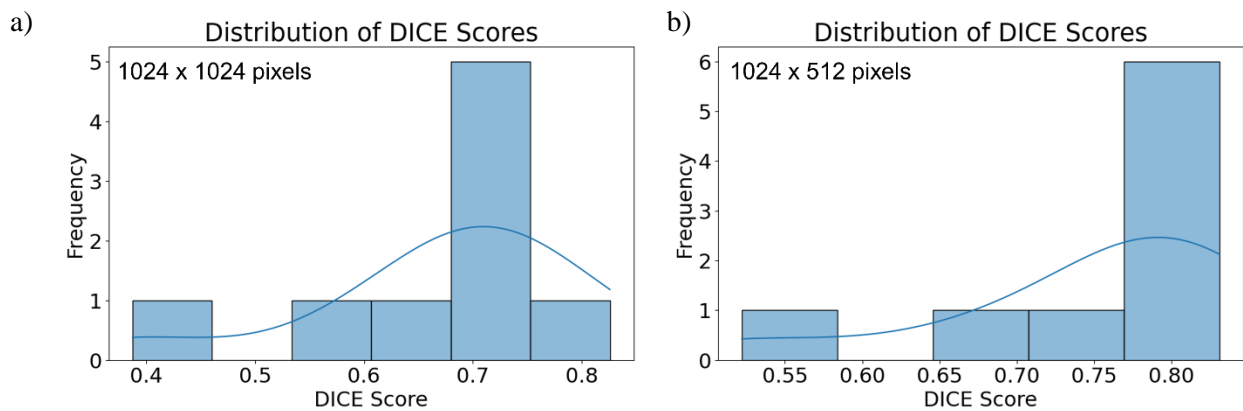
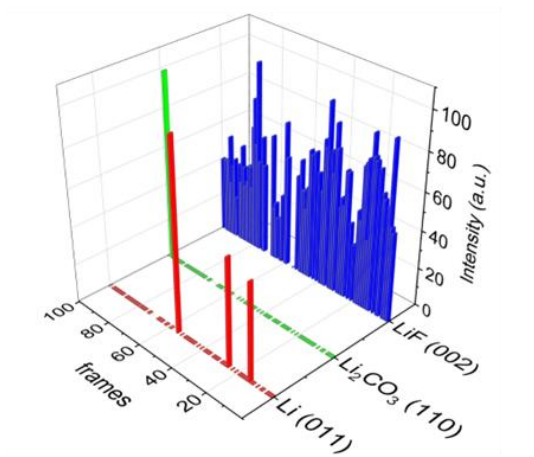


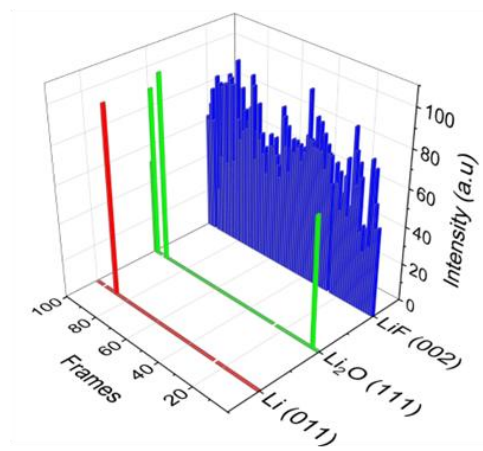
Figure S12. Dice score distribution of the model trained with (a) 1024 x 1024 pixels (b) 1024 x 512 pixels

The model trained on 1024 x 512 pixels images demonstrates consistently higher Dice coefficients than the model trained on 1024 x 1024 pixels images. This observation suggests that the reduced image dimensions may be advantageous for improving the model's segmentation performance and accuracy.

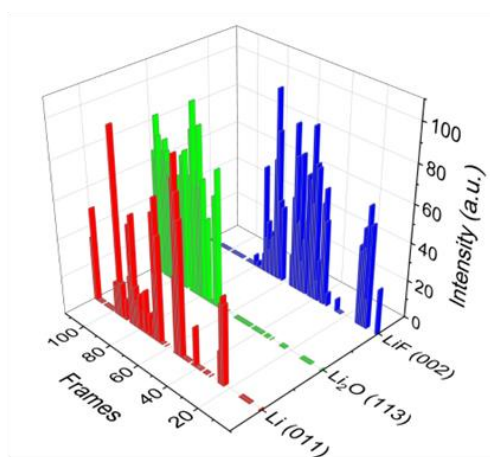
a) LiF at Cryo-T @ $50 \text{ eA}^{-2}\text{s}^{-1}$



b) LiF at Cryo-T @ $200 \text{ eA}^{-2}\text{s}^{-1}$



c) LiF at RT @ $50 \text{ eA}^{-2}\text{s}^{-1}$



d) LiF at RT @ $200 \text{ eA}^{-2}\text{s}^{-1}$

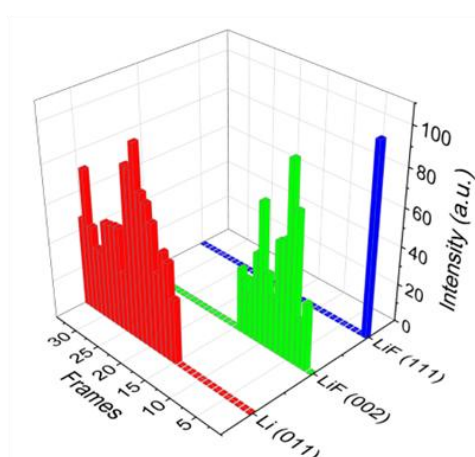


Figure S13. Intensity profiling of analyzed TEM images of LiF at cryo temperature at dose rate of (a) $50 \text{ eA}^{-2} \text{ s}^{-1}$ (b) $200 \text{ eA}^{-2} \text{ s}^{-1}$, and at room temperature at dose rate of (c) $50 \text{ eA}^{-2} \text{ s}^{-1}$. (d) $200 \text{ eA}^{-2} \text{ s}^{-1}$

■ GUI DEVELOPMENT FOR AUTOMATED TEM ANALYSIS

The creation of user-friendly interfaces is increasingly important in scientific software, especially when dealing with non-technical users. Tkinter, a popular Python library for GUI development, was utilized to create a GUI interface for automated TEM analysis in this study. The interface is designed to process TEM images and present the output in a results window. The processed images are displayed under the “SAMPLE NAME” column, and when a processed image is selected, the corresponding TEM image is displayed along with the list of detected components under the “COMPONENTS LIST” column. Each component in the list can be selected to map the region of the component on the TEM image and provide information about the percentage match with the database. This interface is expected to greatly simplify and expedite the analysis of TEM images by providing easy navigation and interactive visualizations. We employ the "multiprocessing" library to undertake the concurrent processing of multiple files. By accepting a parameter encompassing a multitude of file names, we utilize asynchronous parallel processing to expedite the execution of said files.

The developed tool offers several potential advantages over current state-of-the-art analysis programs, particularly when applied to large datasets:

Efficient Batch Processing of TEM Images:

The developed program significantly expedites the analysis of large TEM datasets. It can batch process up to 100 images within 30 minutes, a substantial improvement compared to manual processing using GATAN software, which typically takes around 5 minutes per image. This manual approach can become even more time-consuming depending on the complexity of the FFT images and the number of features to be identified. This program thus offers a valuable tool for

researchers dealing with high-volume TEM data, accelerating their analysis workflow and enabling more efficient extraction of critical information.

Precise and Automated Identification of Periodic Components:

The developed program introduces a novel capability for automatically identifying periodic components in TEM images. By referencing a user-defined database, it assigns the nearest d-spacing material to each detected component in the FFT. This functionality surpasses the capabilities of manual analysis software like GATAN, which lacks automated identification. Furthermore, the high accuracy of the program in detecting periodic components is clearly demonstrated in **Table 1**, highlighting its potential to streamline and enhance the precision of TEM analysis workflows.

Unique Intensity Distribution Profiling:

The developed program introduces a novel and powerful feature for analyzing the evolution of periodic components in TEM images. It generates an intensity distribution profile (**Fig. 5(a)**) (**Fig. S13**) by tracking the intensity of specific features across a series of image slices. This unique capability is not available in any existing analysis software and offers valuable insights into dynamic processes, such as beam damage in LiF samples as demonstrated in this work. This feature is particularly valuable for analyzing in-situ experiments, where large datasets need to be efficiently processed and interpreted.

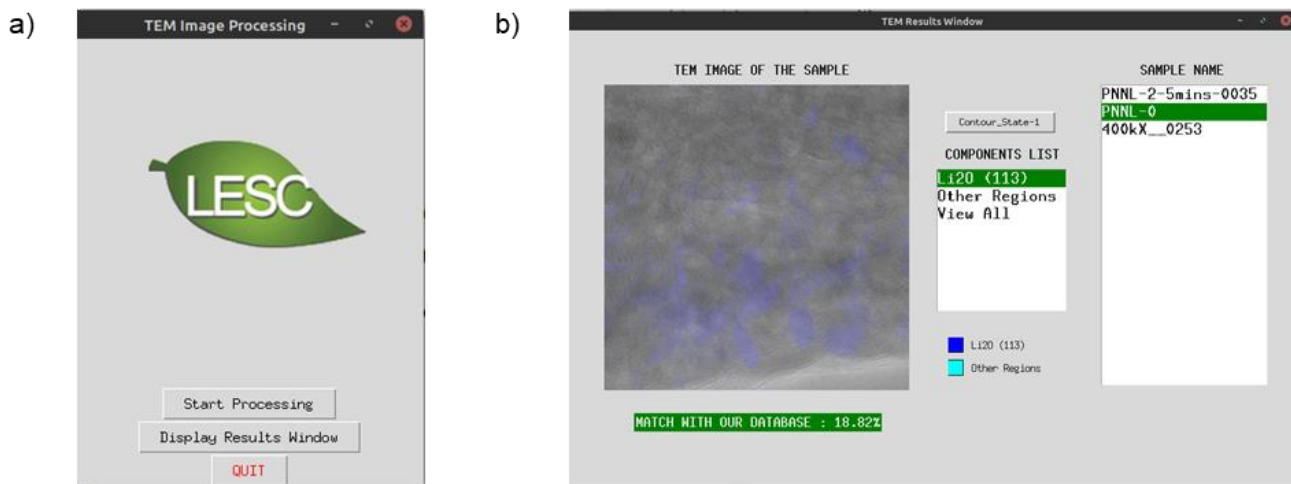


Figure S14. (a) TEM Processing GUI Tool start menu. (b) TEM Results window displaying corresponding components, component mapping on the TEM image.